



# Au decorated hollow ZnO@ZnS heterostructure for enhanced photocatalytic hydrogen evolution: The insight into the roles of hollow channel and Au nanoparticles



Dandan Ma<sup>a</sup>, Jian-Wen Shi<sup>a,\*</sup>, Diankun Sun<sup>a</sup>, Yajun Zou<sup>a</sup>, Linhao Cheng<sup>a</sup>, Chi He<sup>c</sup>, Hongkang Wang<sup>a</sup>, Chunming Niu<sup>a</sup>, Lianzhou Wang<sup>b,\*</sup>

<sup>a</sup> State Key Laboratory of Electrical Insulation and Power Equipment, Center of Nanomaterials for Renewable Energy, School of Electrical Engineering, Xi'an Jiaotong University, Xi'an, 710049, China

<sup>b</sup> Nanomaterials Centre, School of Chemical Engineering and AIBN, The University of Queensland, St. Lucia, Brisbane, QLD, 4072, Australia

<sup>c</sup> Department of Environmental Science and Engineering, School of Energy and Power Engineering, Xi'an Jiaotong University, Xi'an, 710049, China

## ARTICLE INFO

**Keywords:**  
Photocatalysis  
Hydrogen evolution  
Heterostructure  
Hollow channel  
Z-scheme

## ABSTRACT

A new type of Au nanoparticles (NPs) decorated hollow flower-like ZnO@ZnS (HZOS) heterostructure (HS) is elaborately designed as efficient photocatalyst for water splitting application. The optimal Au decorated HZOS exhibits a high hydrogen generation rate of 569.81  $\mu\text{mol}/\text{h}$  (10 mg of catalyst), which is 345, 374 and 11 times higher than that of pristine ZnO (1.65  $\mu\text{mol}/\text{h}$ ), ZnS (1.52  $\mu\text{mol}/\text{h}$ ) and ZnO@ZnS (51.7  $\mu\text{mol}/\text{h}$ ), respectively. Furthermore, its apparent quantum efficiency reaches to 25.47% at the wavelength of 365 nm. The significantly enhanced  $\text{H}_2$  evolution can be attributed to the synergistic effects from the hollow channel structure and the deposited Au NPs. The hollow channel creates a new migration pathway where charge carriers can transfer towards the hollow channel in addition to the outer surface of the photocatalyst, thus significantly reducing the migration distance of charge carriers, suppressing the recombination of photogenerated electrons and holes, and reducing their transfer resistance. The decoration of Au NPs at the interface between ZnO and ZnS not only facilitates the directional migration of charge carriers because of the formation of Schottky barrier, but also works as electron shuttles to form a Z-scheme transfer process, effectively promoting the separation and migration of charge carriers.

## 1. Introduction

Photocatalytic hydrogen evolution from water splitting has received considerable attention owing to the potential to resolve energy and environmental issues [1–3]. In order to obtain photocatalysts with high-efficiency and durability, numerous semiconductors, such as metal oxides [4,5], nitrides [6–8], and sulfides [9–11], have been explored. However, the photocatalytic efficiency of these single semiconductors is still far below the level of practical application [12–14]. In recent years, the heterostructures (HSs) consisting of several semiconductors are attracting more and more attention due to the fact that HSs integrate the merits of several semiconductors into one system, which could overcome the drawbacks of single semiconductors, usually resulting in promoted photocatalytic properties [15–18]. Among a variety of HSs, ZnO/ZnS is becoming a hot spot of research for the photocatalytic  $\text{H}_2$  production from water splitting [19–25] owing to the fact that ZnO and

ZnS have excellent electron mobility, proper energy band positions as well as abundant potential morphologies [20,23]. However, the photocatalytic efficiency of ZnO/ZnS HS is still seriously limited so far, although many efforts have been devoted. The reason can be mainly attributed to the fast recombination of charge carriers [20,23–26]. Therefore, exploring for proper strategies to effectively inhibit charge recombination in this ZnO/ZnS HS has become urgent.

It has been confirmed that the decoration of noble metals on semiconductor is a promising solution to remarkably promote the separation and migration of photogenerated electrons and holes due to the formed Schottky barrier [27–31]. Therefore, the decoration of noble metals on ZnO/ZnS may be a good choice to solve the trouble of charge recombination. Only one report involves Au decorated ZnO/ZnS in literature so far [32], where a sandwich-structured ZnO/ZnS/Au catalyst was prepared by the photodeposition of Au nanoparticles (NPs) on the surface of ZnO/ZnS, which displayed 3.5 times higher solar-to-

\* Corresponding authors.

E-mail addresses: [jianwen.shi@mail.xjtu.edu.cn](mailto:jianwen.shi@mail.xjtu.edu.cn) (J.-W. Shi), [l.wang@uq.edu.au](mailto:l.wang@uq.edu.au) (L. Wang).

hydrogen conversion efficiency than pure ZnO due to the reduction of photogenerated carrier recombination. Furthermore, due to the fact that Au NPs was deposited on the surface of ZnS, the electrons were confirmed to transfer from the conduction band (CB) of ZnS to the CB of ZnO following traditional II-type mechanism [32]. In our previous work, Au NPs located at the interface of C-doped TiO<sub>2</sub> and g-C<sub>3</sub>N<sub>4</sub> transformed the transfer mechanism of charge carriers from the initial II-type into Z-scheme mechanism, significantly improving the photocatalytic H<sub>2</sub> production rate [27,33]. Therefore, for Au decorated ZnO/ZnS, it seems to be possible to transform the transfer mechanism of charge carriers from traditional II-type mechanism into Z-scheme by adjusting the deposition positions of Au NPs, which must be very meaningful to promote the photocatalytic efficiency for H<sub>2</sub> production. However, there is no research report on this aspect yet.

In our recent work, we successfully synthesized ZnO microflowers assembled by many uniform two-dimensional (2D) ZnO nanosheets (NSs) [34]. After an in-situ sulfidation procedure, the surface of ZnO NSs was transformed into ZnS, forming ZnO@ZnS core-shell structure, and the transfer mechanism of charge carriers between ZnO and ZnS was proved to be traditional II-type mechanism [34,35]. On the basis of these studies, in the present work, we firstly design a hollow channel structure by the partial etching of the ZnO core, then deposit Au NPs into the obtained hollow ZnO@ZnS by a simple chemical deposition method (the synthesis route is shown in **Scheme 1**). As a result, the well-designed catalyst (hollow ZnO@ZnS decorated with Au) exhibits remarkably enhanced H<sub>2</sub> evolution rate of 569.81 μmol/h, which is 345, 374 and 11 times higher than that of pristine ZnO (1.65 μmol/h), ZnS (1.52 μmol/h) and ZnO@ZnS (51.7 μmol/h), respectively. The reasons for significantly enhanced photocatalytic H<sub>2</sub> evolution are further investigated in details to understand synergistic effects of the hollow channel structure and the deposited Au NPs on photocatalytic performance.

## 2. Experimental section

### 2.1. Materials

Zinc nitrate (Zn(NO<sub>3</sub>)<sub>2</sub>·6H<sub>2</sub>O) was obtained from Chengdu kelon chemical reagent factory, China. Hexamethylene tetramine (HMTA), terephthalic acid (TA), thiourea (CH<sub>4</sub>N<sub>2</sub>S), sodium sulfite anhydrous (Na<sub>2</sub>SO<sub>3</sub>), sodium hydroxide (NaOH), potassium hydroxide (KOH) and

sodium sulfate (Na<sub>2</sub>SO<sub>4</sub>) were obtained from Sinopharm Chemical Reagent Co., Ltd. Sodium sulfide (Na<sub>2</sub>S·9H<sub>2</sub>O) was obtained from Tianjin Tianli Chemical Reagent Co., Ltd, China. Chloroauric acid solution (HAuCl<sub>4</sub>·4H<sub>2</sub>O 10 wt. % in H<sub>2</sub>O) was ordered from Shanghai Macklin Biochemical Co., Ltd, China. Chloroplatinic acid solution (H<sub>2</sub>PtCl<sub>6</sub> 8 wt. % in H<sub>2</sub>O) was ordered from Shanghai Aladdin Bio-Chem Technology Co., Ltd, China. All reagents were analytical grade and used as received without further purification. Deionized water with resistivity of 18.2 MΩ cm was used throughout the experiments.

### 2.2. Synthesis of ZnO@ZnS core@shell HSs

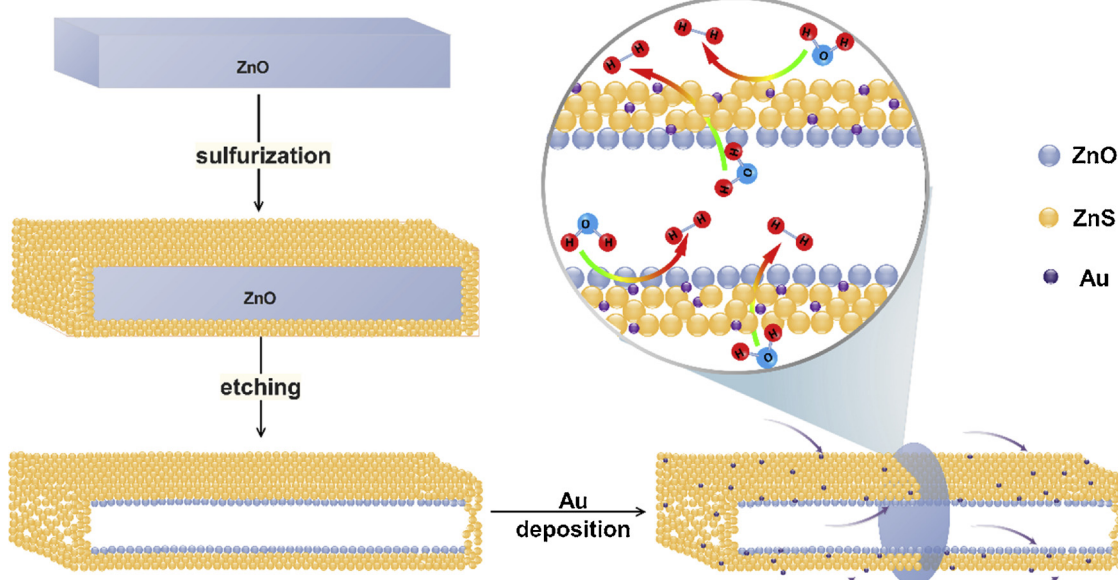
The ZnO@ZnS HSs were prepared by an in-situ sulfidation procedure from flowerlike ZnO reported in our former work [35]. In typical, 100 mg of thiourea was dissolved in 20 mL of water, and then 100 mg of flowerlike ZnO was added in and dispersed by ultrasonic. The resultant mixture was then transferred to an 80 mL Teflon autoclave and maintained at 180 °C for 20, 40 and 60 min to initiate in-situ sulfidation reaction, resulting in three ZnO@ZnS HSs with different sulfidation degree. For convenience, the obtained samples were labeled as ZOS-x where x stood for the sulfidation time (min).

### 2.3. Fabrication of hollow ZnO@ZnS HSs

Hollow ZnO@ZnS HSs were obtained by an alkali etching method [36]. Firstly, 20 mg of ZOS-40 was added into 25 mL of KOH solution (2 M, 4 M and 6 M, respectively). After constant stirring for 20 min, the products were collected by centrifugation, washed with deionized water for three times and dried at 60 °C in air, resulting in three hollow ZnO@ZnS HSs with different etching degree. For convenience, the obtained hollow ZnO@ZnS HSs were denoted as HZOS<sub>y</sub>, where y was the concentration of KOH.

### 2.4. Synthesis of Au-decorated hollow ZnO@ZnS HSs

Au-decorated hollow ZnO@ZnS was prepared through a chemical deposition procedure. In brief, 10 mg of HZOS<sub>y</sub> powder was suspended in 10 mL of water by ultrasonic, and then different amount of 10 wt% chloroauric acid solution (HAuCl<sub>4</sub>·4H<sub>2</sub>O, 6.3 mg, 8.4 mg and 10.5 mg) was added into the suspension with stirring for 10 min. The obtained gray products were collected by centrifugation, washed with deionized



**Scheme 1.** Schematic illustration for the synthetic route of Au decorated hollow channel structure ZnO@ZnS.

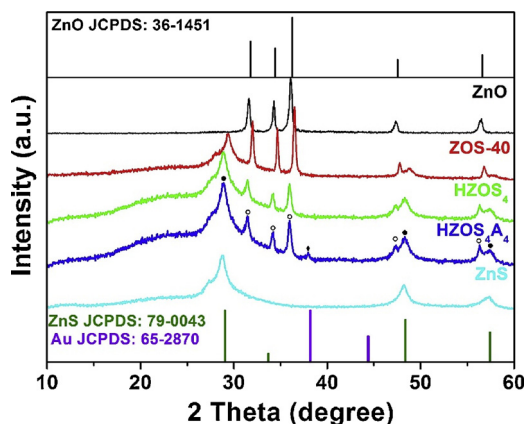


**Fig. 1.** XRD patterns of the as-synthesized ZnO, ZOS-40, HZOS<sub>4</sub>, HZOS<sub>4</sub>A<sub>4</sub> and ZnS (JCPDS 36-1451, 79-0043, and 65-2870 correspond to the standard diffraction cards of hexagonal ZnO, cubic ZnS, and cubic Au, respectively, which are separately marked with circle, black dot and rhombus in the XRD pattern of HZOS<sub>4</sub>A<sub>4</sub>).

water for three times and dried at 60 °C in air, resulting in Au-decorated hollow ZnO@ZnS HSs with three different amounts of Au. The weight ratios of Au to HZOS<sub>y</sub> were 3, 4, and 5 wt. %, respectively. For convenience, the samples were labeled as HZOS<sub>y</sub>A<sub>z</sub> where z stood for the weight ratio of Au.

In addition, Au decorated ZnS (ZnS-Au) and ZnO (ZnO-Au) were prepared for comparison. ZnS was prepared by the complete in-situ sulfidation of ZnO by prolonging the sulfidation time to 120 min, which is the same as our former report [35]. Then, ZnS-Au was fabricated with the same method (chemical deposition procedure) by changing HZOS<sub>y</sub> to ZnS. ZnO-Au was prepared through a photo deposition procedure [36,37]. In typical, 10 mg of ZnO was suspended in 10 mL of water by ultrasonic, then a certain amount of chloroauric acid solution was added and followed by irradiation under a 225 W Xe lamp for 30 min with stirring. The obtained dark gray product was collected by centrifugation, washed with deionized water for three times and dried at 60 °C in air, resulting in ZnO-Au.

Additionally, ZOSA<sub>4</sub>-ET was also fabricated for comparison. In brief, 20 mg of ZOS-40 powder was suspended in 20 mL of water by ultrasonic, and then 16.8 mg of 10 wt% HAuCl<sub>4</sub>·4H<sub>2</sub>O was added with stirring for 10 min, result in Au decorated ZOS-40 (ZOSA<sub>4</sub>). Subsequently, the suspension was collected by centrifugation, and then dispersed into 25 mL of KOH solution (4 M) with constant stirring for 20 min. Afterward, the product was collected by centrifugation, washed with deionized water for three times and dried at 60 °C in air, resulting in ZOSA<sub>4</sub>-ET.

## 2.5. Photocatalytic hydrogen evolution

The photocatalytic hydrogen evolution from water splitting was carried out in a top-irradiation quartz cell connected to a closed glass gas circulation system (CEL-SPH2N, Beijing). 10 mg of the photocatalyst was dispersed in 25 mL of aqueous solution with 0.35 M of sodium sulfide and 0.25 M of sodium sulfite anhydrous as sacrificial agent. The reaction temperature was maintained around 6 °C A 225 W xenon arc lamp (CEL-PF300-T8) was used as light source (320–780 nm). The amount of H<sub>2</sub> evolved under irradiation was determined via a TCD gas chromatograph (GC-9720).

## 2.6. Characterization

X-ray diffraction (XRD) patterns were recorded on a Philips X'pert Multipurpose X-ray diffraction system using Cu K<sub>α</sub> radiation in step mode between 10° and 60°. Scanning electron microscopy (SEM)

images were taken with a field emission scanning electron microscope (FESEM, Quanta 250 FEG). Transmission electron microscopy (TEM) images were taken on a JEOL JEM-2100 F microscope operating at a voltage of 200 kV. Energy dispersive spectroscopy (EDS) mapping were observed by a transmission electron microscope (FEI Tecnai G2 F30 S-Twin, USA) with an accelerating voltage (300 kV). UV – Visible diffuse absorption spectra (UV-vis DRS) were recorded with a UV-vis-NIR spectrometer (JASCO, V-670) with an integrating sphere. X-ray photoelectron spectroscopy (XPS) analyses were performed on X-ray Photoelectron Spectrometer (ESCALAB Xi+) with aluminum K<sub>α</sub> radiation. The specific surface area of the samples was characterized using Micromeritics Tristar 2000 instrument at 77 K and calculated by the Brunauer Emmett Teller (BET) method. The photoluminescence (PL) spectra were measured by a fluorescence spectrometer (Edinburgh Instruments FLS 980). The electrochemical analyses were carried out in a conventional three-electrode system and recorded on a CHI 660 E electrochemical workstation (Shanghai, China). Ag/AgCl used as reference electrode and Pt slice as counter electrode. Fluorine-doped tin oxide (FTO, 7Ω per square) decorated with catalyst was used as the working electrode. The electrolyte was Na<sub>2</sub>SO<sub>4</sub> solution (0.1 M). Light on and off was controlled by a shutter in every 20 s to test the photocurrent response. Zeta potential experiment was determined on Malvern Zetasizer 3000 HS at 25 °C. Electrochemical impedance spectroscopy (EIS) measurement was carried out in the frequency range from 0.1 Hz to 10<sup>5</sup> Hz with a bias voltage of 0.5 V. Mott-Schottky (M-S) plots were collected by conducting impedance-potential spectroscopy at 10 kHz in 0.1 M Na<sub>2</sub>SO<sub>4</sub> solution over a range of potentials from -0.7 to -0.2 V versus silver chloride electrode (Ag/AgCl).

## 2.7. Analysis of hydroxyl radicals

Hydroxyl radicals (·OH) generated over the samples were detected by photoluminescence (PL) by using terephthalic acid (TA) as a probe molecule. In a typical procedure, 10 mg of the sample was dispersed in an aqueous solution (20 mL) of 5 × 10<sup>4</sup> M TA and 2 × 10<sup>3</sup> M NaOH. The mixture was then irradiated by using a 225 W Xe lamp (CEL-PF300-T8) for 30 min with stirring. Afterward, the solid catalyst was separated by centrifugation and the upper solution was analyzed on a FLS980 fluorescence spectrometer with an excited wavelength at 315 nm.

## 3. Results and discussion

**Fig. 1** shows the XRD patterns of the as-synthesized samples. The pure ZnO displayed the characteristic peaks of hexagonal ZnO (JCPDS36-1451) [33,35], and all the diffraction peaks were sharp and strong, indicating its good crystallinity. Three new peaks at 29.06, 48.37 and 57.42° appeared in the XRD pattern of ZOS-40 due to the sulfidation treatment, which can be indexed to (111), (220) and (311) planes of cubical zinc blende structure ZnS (JCPDS no.79-0043) [38]. The peak positions of ZnO shifted slightly to higher angle in comparison with its standard card, which can be ascribed to the small change of lattice state resulted from the interaction between ZnO and the new formed ZnS. The peak intensity of ZnO decreased a lot in the XRD pattern of HZOS<sub>4</sub> due to the etching treatment, implying the ZnO was gradually consumed resulted from the etching of KOH solution [36,37]. Furthermore, the peak positions of ZnO shifted back to lower angle and coincided well with the standard card of hexagonal ZnO, indicating that the interaction between ZnO and ZnS is gradually relieved due to the consumption of ZnO. A new peak at 38.18° appeared in the XRD pattern of HZOS<sub>4</sub>A<sub>4</sub>, which can be assigned to (111) plane of Au (JCPDS no. 65-2870), suggesting that the deposition of Au NPs has been realized. The effects of sulfidation, etching, and Au deposition on the crystal structure of samples are presented in detail in **Fig. S1** (Supporting Information).

**Fig. S2** (Supporting Information) illustrates the morphology evolution of the samples by SEM. The pure ZnO exhibited the flowerlike structure with a diameter of about 3 μm (**Fig. S2a**), which were

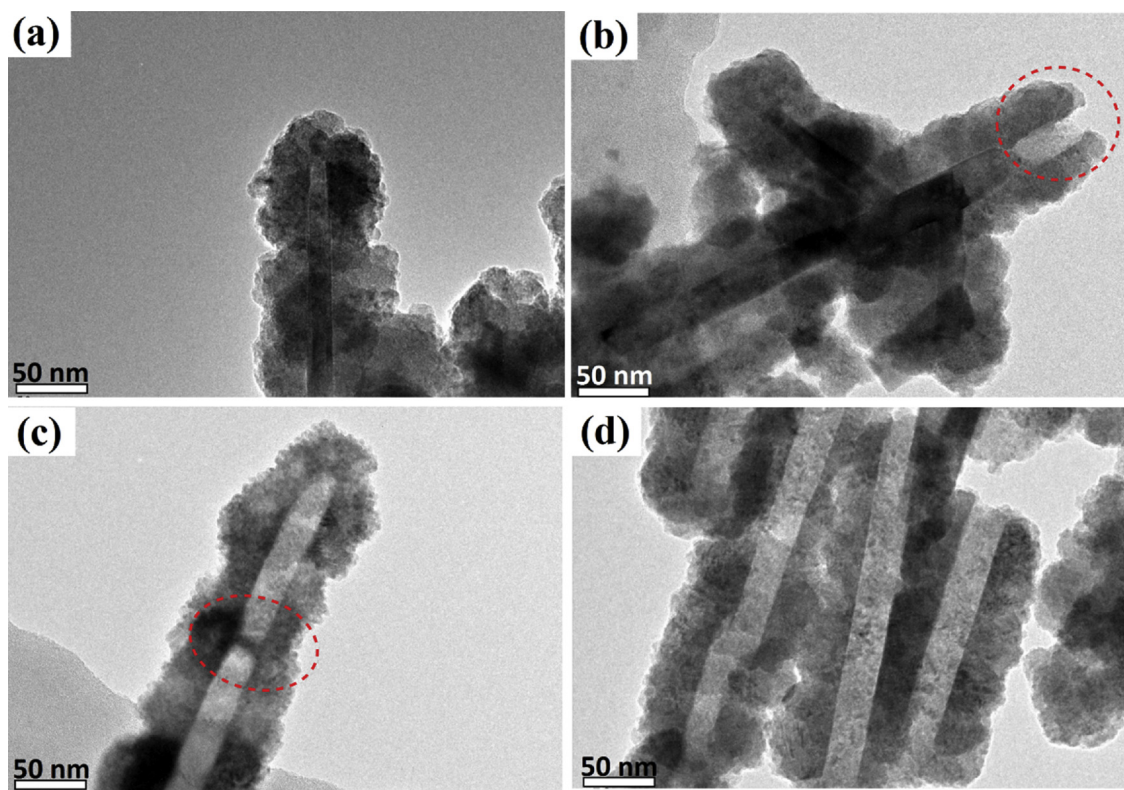


Fig. 2. High-magnification TEM images of samples: ZOS-40 (a), HZOS<sub>2</sub> (b), HZOS<sub>4</sub> (c) and HZOS<sub>6</sub> (d).

consisted of smooth ZnO NSs with the average thickness of about 25 nm (Fig. S2b). ZOS-40 maintained a flowerlike morphology at macro level, but the smooth surface of ZnO NSs was sulfurized into a fluffy structure, which can be attributed to the newly generated ZnS nanoparticles (Fig. S2c). In addition, the thickness of nanosheets significantly increased to 60~80 nm (Fig. S2d), implying that these new ZnS nanoparticles must be very loose, which is very conducive to the deposition of Au NPs into the interior. The morphology remained essentially unchanged after etching by KOH solution (Fig. S2e and f). After the loading of Au NPs, many tiny bright nanoparticles attached on the surface of sample were observed (Fig. S2g and h), indicating the successful deposition of Au NPs.

In order to explore the formation process of the hollow structure, the TEM analysis of HZOS<sub>y</sub> with different etching degree was carried out. As shown in Fig. 2a, the ZOS-40 was composed of ZnO core and ZnS shell before the etching. After etching for 20 min in the 2M of KOH solution, the end of the ZnO nanosheet was etched a little (marked with a red dot circle in Fig. 2b). When the concentration of KOH solution increased to 4 M, the whole ZnO nanosheet was almost completely hollowed out with a little left at the middle of the channel (marked with a red dot circle in Fig. 2c). When the concentration of KOH solution further increased to 6 M, ZnO nanosheet completely disappeared, forming the hollow channel structure consisted of ZnS (Fig. 2d). During the whole etching process, the flowerlike morphology did not change, which can be confirmed by the TEM images with low magnification (Fig. S3).

As a typical sample, HZOS<sub>4</sub>A<sub>4</sub> was further characterized by TEM to reveal its microstructures. The HZOS<sub>4</sub>A<sub>4</sub> still maintained the flower-like morphology (Fig. 3a). A distinct contrast between the inner cavity and the outer shell can be observed from Fig. 3b, demonstrating that ZnO core is hollowed out while ZnS shell remains to form hollow channel structure. Moreover, a large number of small dark dots through the whole shell can be observed (Fig. 3b-d), which is ascribed to the deposited Au NPs. The statistical size distribution of Au NPs was *ca.* 2~4 nm (Fig. 3e), which is much smaller than some reports [32,39]

where photo deposition method was utilized rather than chemical deposition method used in this work (compared with photo deposition, the advantages of chemical deposition are confirmed and described in detail in Supporting Information (Figs. S4 and S5)). Three lattice fringes of 0.28, 0.31 and 0.23 nm, corresponding to (100) plane of hexagonal wurtzite ZnO, (111) plane of cubic ZnS and (200) plane of Au, respectively [36–41], can be observed from the HRTEM image of HZOS<sub>4</sub>A<sub>4</sub> (Fig. 3d), suggesting that HZOS<sub>4</sub>A<sub>4</sub> contains ZnO, ZnS and Au. Furthermore, the intimate connected ZnO-Au-ZnS and ZnS-Au interfaces were detected (Fig. 3d-1 and d-2), suggesting that there are two kinds of positions for the deposition of Au NPs, the interface between ZnO and ZnS, and the surface of ZnS [29,33,36]. The hollow channel structure can also be confirmed by the scanning TEM energy dispersive spectroscopy (STEM-EDS) mapping. As shown in Fig. 3f-i, a clearly hollow channel was formed, demonstrating that ZnO nanosheet has been etched and disappeared from the position of core. The purple dots of Au atoms were distributed throughout the whole shell, indicating its uniform distribution among the majority elements of Zn and S atoms.

The XPS of HZOS<sub>4</sub>A<sub>4</sub> was carried out to further explore the surface elemental composition and valence state (Fig. S6). The survey XPS spectrum (Fig. S6a) verified the presence of Zn, O, S, and Au. Fig. S6b show the high-resolution XPS spectra of Zn 2p, where two peaks at 1022.19 and 1045.06 eV were observed, corresponding to Zn 2p<sub>3/2</sub> and Zn 2p<sub>1/2</sub>, respectively, suggesting the normal oxidation state of Zn<sup>2+</sup> [43,44]. The two other peaks at 1021.72 eV and 1049.56 eV might be caused by the interaction between ZnS, ZnO and Au. The coexistence of lattice oxygen species (530.62 eV) and chemisorbed oxygen species (532.23 eV) in O 1s spectrum (Fig. S6c) confirmed the existence of ZnO in the part-etching sample [37]. The formation of ZnS can be verified from Fig. S6d, where the binding energy of S 2p appeared at about 161.58 eV and 162.84 eV, which are the typical values for metal sulfides [45,46]. Two significant binding energy peaks at 84.26 and 88.27 eV appeared in the XPS spectrum of Au 4f (Fig. S6e), which correspond to the electronic states of Au 4f<sub>7/2</sub> and Au 4f<sub>5/2</sub>, respectively, confirming the existence of Au NPs in HZOS<sub>4</sub>A<sub>4</sub> [33]. The

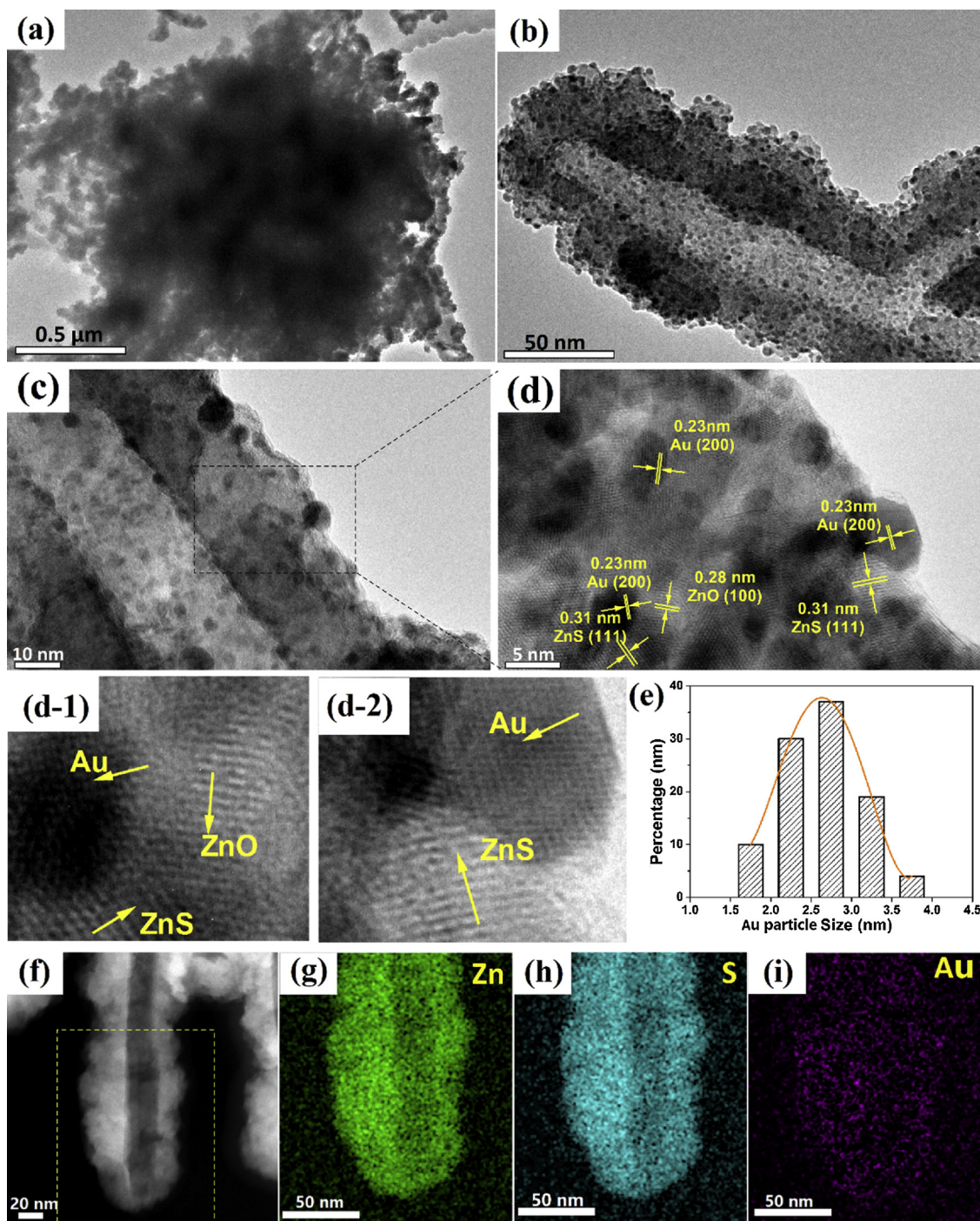


**Fig. 3.** TEM (a–c) and HRTEM (d) images of HZOS<sub>4</sub>A<sub>4</sub>: (d-1) and (d-2) are the different interfaces observed in the HRTEM; (e) is the measured size distribution of Au NPs; (f), (g), (h), and (i) are the STEM-EDS images.

amount of Au in HZOS<sub>4</sub>A<sub>4</sub> determined by ICP-MS measurement was 3.75 wt.%, which approximately equals to the experimental dosage (4 wt.%), indicating that all the added HAuCl<sub>4</sub>·4H<sub>2</sub>O has been deposited on the HZOS<sub>4</sub> substrate as Au NPs by the chemical deposition method. Along with Au 4f<sub>5/2</sub>, a peak at 91.32 eV appeared, which can be ascribed to the Zn 3p [32].

The optical absorption properties of the samples were investigated by UV-vis absorption spectra. As shown in Fig. 4a, ZnO presented strong absorption in UV light region (200~400 nm) and very weak absorption (almost no absorption) in visible light region (400~800 nm) with a very steep absorption edge at about 400 nm due to its large bandgap (3.2 eV) [43]. Compared with ZnO, the absorption edge of ZnS

shifted towards short wavelength (about 365 nm) owing to its broader bandgap (3.7 eV) [47]. Due to the generation of ZnS, the absorption of ZOS-40 in UV light region dropped a little bit in comparison with ZnO, but the steep absorption edge still maintained at about 400 nm. After a partial of ZnO was hollowed out, HZOS<sub>4</sub> exhibited a certain weak absorption in visible light region (400~800 nm) with the invariable absorption edge. As for HZOS<sub>4</sub>A<sub>4</sub>, the absorption in visible light region was significantly enhanced due to the surface plasmon resonance (SPR) effect of Au NPs [32,48]. The corresponding Tauc plot is displayed in Fig. S7, and the bandgap values of all samples determined by the Tauc/David-Mott equation  $\alpha(h\nu) = A(h\nu - E_g)^{n/2}$  (where  $\alpha$ ,  $\nu$ ,  $E_g$ , and  $A$  are the absorption coefficient, light frequency, band gap energy, and a

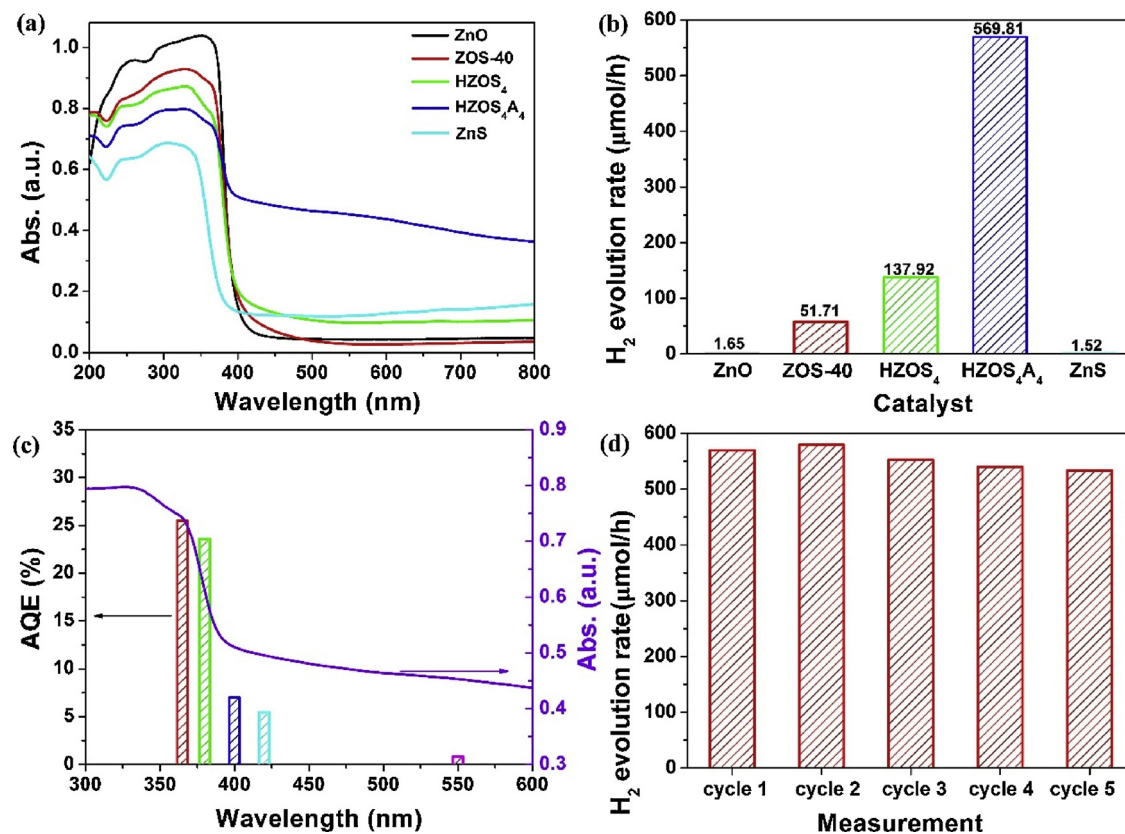


**Fig. 4.** The UV-vis absorption spectra (a) and the comparison of the photocatalytic hydrogen evolution (b) over ZnO, ZOS-40, HZOS<sub>4</sub>, HZOS<sub>4</sub>A<sub>4</sub> and ZnS (10 mg of catalyst); The wavelength-dependent AQE of H<sub>2</sub> evolution (c) and the cycling stability of photocatalytic H<sub>2</sub> evolution in 20 h (evacuation every 4 h) over HZOS<sub>4</sub>A<sub>4</sub> (d).

constant, respectively) [40,49] a S1 (Considering that both ZnO and ZnS are the direct band gap semiconductors [50–52],  $n = 1$  was adopted in the equation).

Fig. 4b shows the hydrogen evolution rate over the samples. Both ZnO and ZnS presented low hydrogen evolution rate (1.65 and 1.52 μmol/h, respectively). ZOS-40 exhibited a much higher hydrogen evolution rate (51.7 μmol/h) than single ZnO and ZnS, which can be attributed to the formation of ZnO-ZnS heterojunction, facilitating the transfer and separation of photogenerated charge carriers. After a part of the ZnO core became hollow, the hydrogen evolution rate over HZOS<sub>4</sub> was significantly enhanced (137.92 μmol/h), which is more than 2.7 times higher than that of ZOS-40. The reason can be ascribed to the fact that the photogenerated electrons accumulated on ZnO core can be rapidly consumed by water flowing into the hollow channel structure to trigger hydrogen evolution reaction. [53,54] It is worth noting that the hydrogen evolution rate was further improved to 569.81 μmol/h when HZOS<sub>4</sub>A<sub>4</sub> was utilized as photocatalyst, which is more than 4 times higher than that of HZOS<sub>4</sub>, suggesting the deposited Au NPs also contributes photocatalytic H<sub>2</sub> evolution. We carefully consulted the hydrogen evolution rate over ZnO-ZnS based HSs reported in literatures (Table S2) and found that the hydrogen evolution rate over HZOS<sub>4</sub>A<sub>4</sub> in this work is the highest value. The effects of sulfidation, etching, and Au deposition on the hydrogen evolution rate of samples are presented in detail in Fig. S8 (Supporting Information).

The apparent quantum efficiency (AQE) of HZOS<sub>4</sub>A<sub>4</sub> at different wavelengths was measured. As shown in Fig. 4c, the AQE values exhibited the coincident change with the UV-vis absorption spectrum, and the highest AQE reached to 25.47% at the wavelength of 365 nm (Table S3). In order to investigate the durability and stability of the as-obtained photocatalyst, the performance of cyclic hydrogen production over HZOS<sub>4</sub>A<sub>4</sub> was measured. As shown in Fig. 4d, the H<sub>2</sub> evolution rate

was maintained for five cycles (20 h) without obvious decay, indicating its good durability and stability. Furthermore, there is no obvious change in the XRD results of HZOS<sub>4</sub>A<sub>4</sub> before and after photocatalytic reaction (Fig. S9), further demonstrating the good durability and stability of HZOS<sub>4</sub>A<sub>4</sub> for the photocatalytic H<sub>2</sub> evolution.

Fig. 5a shows the photoluminescence (PL) spectra of the samples. It can be observed that pure ZnO displayed high PL intensity, indicating the serious recombination of carriers, which is harmful to the photocatalytic reaction. The PL intensity over ZOS-40 decreased a little due to the formation of ZnO-ZnS heterojunction. After etching with KOH, the PL intensity over HZOS<sub>4</sub> exhibited a visible decline, indicating that the recombination of internal charge carriers is restrained to a certain degree due to the partial removal of ZnO core. It should be noticed that the loading of Au NPs resulted in drastic decline of PL intensity (HZOS<sub>4</sub>A<sub>4</sub>), implying that Au plays an important role in the efficient inhibition of the recombination of photogenerated holes and electrons [46,47].

Fig. 5b presents the results of the transient photocurrent test. Pure ZnO and ZnS showed the lowest photocurrent response owing to the quick recombination of photogenerated charge carriers. The photocurrent response of ZnO was higher than that of ZnS, which is because of the relative smaller band gap. The photocurrent intensity of ZOS-40 increased a little on the basis of pure ZnO, which can be ascribed to the formed ZnO@ZnS HS. The HZOS<sub>4</sub> exhibited obviously improved photocurrent intensity due to the hollow channel structure, implying that the hollow structure contributes to the separation and transfer of photogenerated electrons and holes. Compared to HZOS<sub>4</sub>, HZOS<sub>4</sub>A<sub>4</sub> exhibited stronger photocurrent response, which can be attributed to the efficient separation and transfer of photogenerated charge carriers resulting from the decoration of Au NPs. The results of EIS measurement are shown in Fig. 5c. The HZOS<sub>4</sub> displayed a smaller arc radius

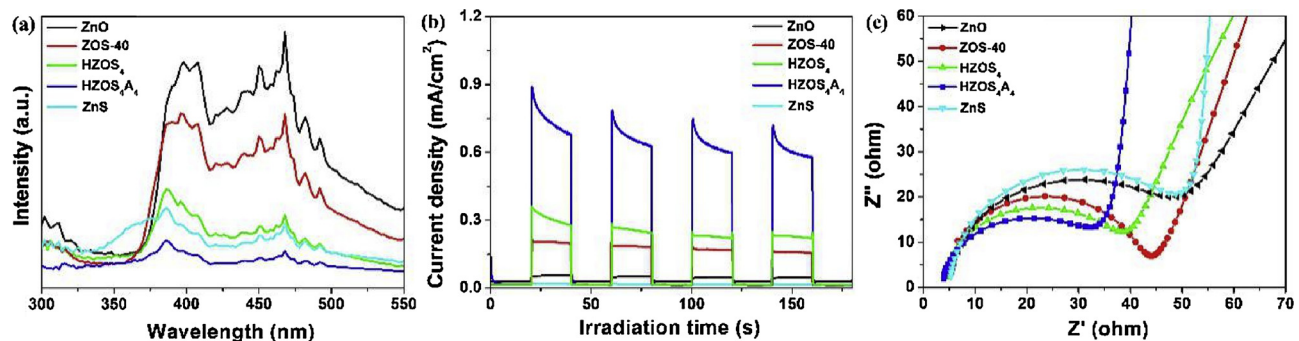
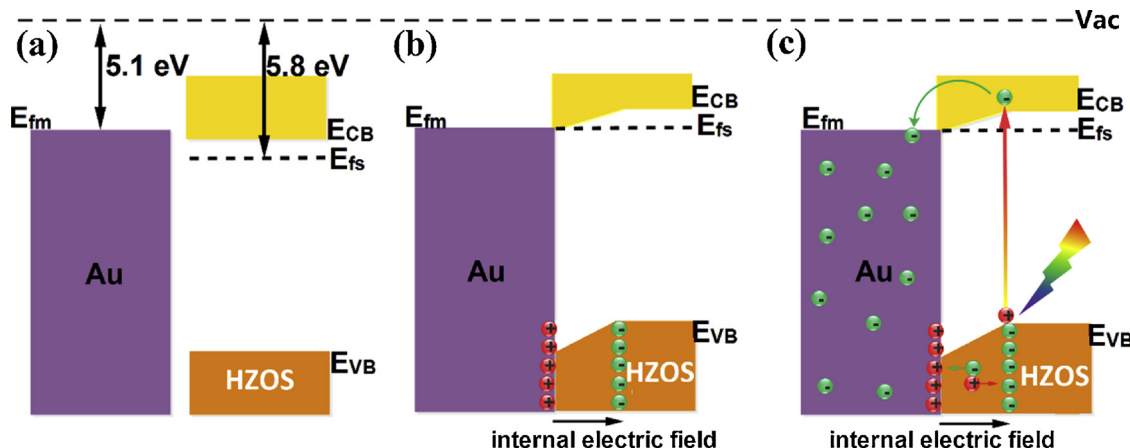


Fig. 5. The PL spectra at the excitation wavelength of 270 nm (a), the photocurrent-time (i-t) curves (b) and the EIS (c) of the samples under xenon lamp (225 W, 320–780 nm).



Scheme 2. Schematic band illustrations of the band structure alignments of Au NPs and HZOS<sub>4</sub> (a), the formation of Schottky junction and internal electric field between Au NPs and HZOS<sub>4</sub> (b), the charge transfer in the Au decorated HZOS<sub>4</sub> under simulated solar light irradiation (c).

than ZOS-40, suggesting that the hollow channel structure is helpful to reduce the charge transfer resistance. The arc radius was further reduced over HZOS<sub>4</sub>A<sub>4</sub> (the smallest arc radius among all the tested samples), indicating the Au deposition can further reduce the charge transfer resistance.

Due to the hollow channel structure, HZOS<sub>4</sub> (137.92 μmol/h) presented more than 22 times higher H<sub>2</sub> evolution rate than that of ZOS-40 (5.17 μmol/h). Therefore, it is reasonable to state that the hollow channel structure in ZnO@ZnS facilitates the photocatalytic H<sub>2</sub> evolution. Fig. S10 and Table S4 show the results of nitrogen adsorption-desorption measurement. The specific surface area (S<sub>BET</sub>) of ZOS-40 was 25.41 m<sup>2</sup>/g, which was increased to 28.35 m<sup>2</sup>/g of HZOS<sub>2</sub> and 34.88 m<sup>2</sup>/g of HZOS<sub>4</sub>, respectively, due to the increase in the etching degree. Higher S<sub>BET</sub> provides more surface reaction active sites for the generation of H<sub>2</sub>. Furthermore, the etching process endows the catalyst with loose hollow channel, thus the reactant and product molecules can be quickly adsorbed and released from the surface of both outer and inner surface of the catalyst, which can improve the utilization of surface reactive sites and thus further accelerate the generation of H<sub>2</sub>. Due to the formation of the hollow channel structure resulted from the partial etching of ZnO core, a new migration direction of photo-generated carriers has been created where carriers can transfer towards the hollow channel besides the outer surface. Thus, the migration distance of the charge carriers from the inside to the surface of catalyst is effectively shortened, which helps to suppress the recombination of photogenerated electrons and holes, promote their separation and migration, and reduce their transfer resistance.

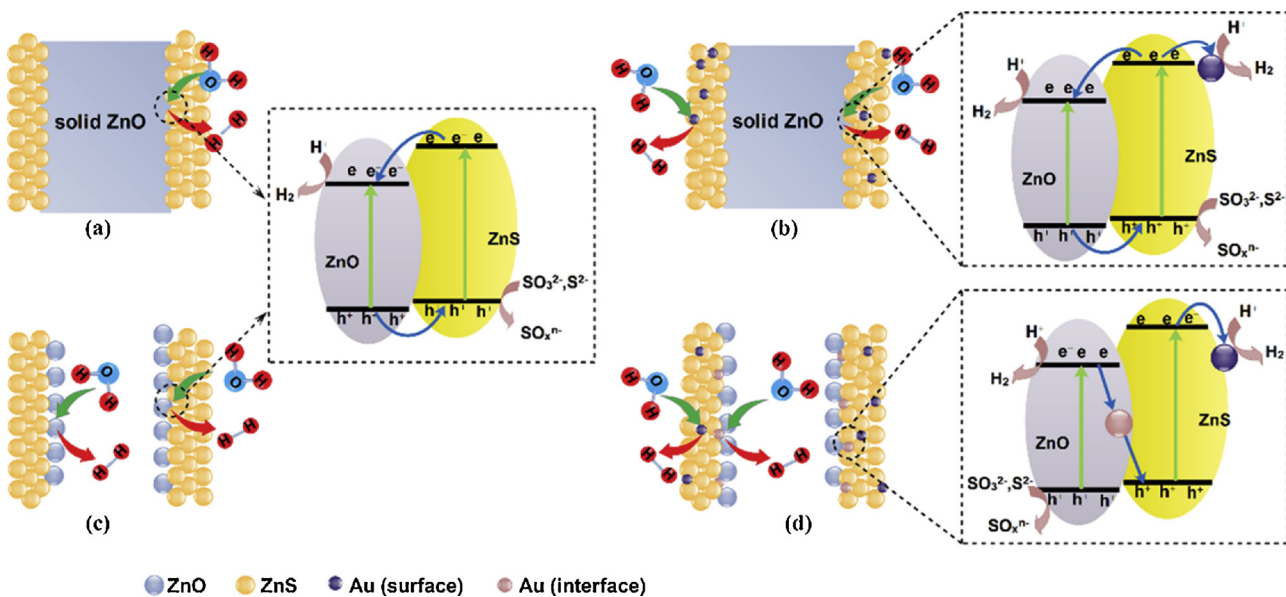
From the results of characterizations and the deposition method of Au NPs, it can be deduced that Au NPs have two kinds of depositional positions, the surface of ZnS and the interface between ZnO and ZnS.

The two situations are discussed separately to get in-depth understanding on the role of Au NPs. For the Au NPs deposited on the surface of ZnS, the HZOS<sub>4</sub> is supposed as one semiconductor. As well known, when a metal intimately contacts with a semiconductor, a Schottky junction will be formed due to the difference between their work functions, which will lead to the bending of energy band to facilitate the separation of electrons and holes [55,56]. In order to obtain the position of CB and valence band (VB), the Mott-Schottky (M-S) plots of the samples were further collected. As shown in Fig. S11, all the samples presented a positive slope, indicating the characteristic of n-type semiconductors. The flat-band potential values of the samples were calculated using the Mott-Schottky equation by extrapolating the X-intercept to  $1/C^2 = 0$ . Since the flat band potential of the n-type semiconductors can be considered approximately as the conduction band edge, the corresponding band potentials can be calculated according to the formula:  $E_g = E_c - E_v$  [36], where  $E_g$ ,  $E_c$  and  $E_v$  are the band gap energy, conduction band energy and valence band energy, respectively. According to the results of the calculation, the corresponding band positions are summarized in Table S1. Based on the  $E_g$  and  $E_{CB}$  values, the work function (W) of HZOS<sub>4</sub> can be calculated using the following equations [55,57]:

$$E_{CB} = -W + 0.5 E_g \quad (1)$$

$$E_{VB} = -W - 0.5 E_g \quad (2)$$

As shown in Scheme 2a, the calculated work function of HZOS<sub>4</sub> is 5.81 eV, larger than that of Au ( $W_{Au} = 5.1$  eV). When HZOS<sub>4</sub> contacts with Au NPs (Scheme 2b), electrons will transfer from Au (higher Fermi level) to HZOS<sub>4</sub> (lower Fermi level) to build up an equilibrium state between the Fermi levels of Au and HZOS<sub>4</sub>. As a result, the conduction band of HZOS<sub>4</sub> bends downward to form a Schottky barrier [55–58].



**Scheme 3.** The comparison diagram on the roles of the hollow channel structure and the deposited Au NPs played in the transfer mechanism of charge carriers and the photocatalytic hydrogen evolution position.

Moreover, the charge migration creates an internal electric field in the space charge region in  $\text{HZOS}_4$  following from Au to  $\text{HZOS}_4$  [59]. When  $\text{HZOS}_4$  is excited by irradiation (Scheme 2c), electrons jump to the CB and holes remain on the VB of  $\text{HZOS}_4$ , and the internal electric field formed between Au and  $\text{HZOS}_4$  can powerfully drive the electrons to migrate towards Au NPs, while the formed Schottky barrier can efficiently prevent the electrons drift from Au back to  $\text{HZOS}_4$ , thus efficiently boosting the separation and migration of photogenerated electrons and holes. The holes remained on the VB of  $\text{HZOS}_4$  will be consumed by sacrificed agents while the electrons accumulated on the surface Au will reduce  $\text{H}^+$  to  $\text{H}_2$ , resulting in the enhanced photocatalytic  $\text{H}_2$  evolution rate.

To get in-depth understanding to the role of Au NPs deposited at the interface between ZnO and ZnS, the detection of generated  $\cdot\text{OH}$  was carried out over  $\text{HZOS}_4$ , ZOSA<sub>4</sub>-ET,  $\text{HZOS}_4\text{A}_4$ ,  $\text{HZOS}_6$  and  $\text{HZOS}_6\text{A}_4$  (ZOSA<sub>4</sub>-ET was prepared by etching ZOSA<sub>4</sub> with 4 M of KOH solution). As shown in Fig. S12a, after the same irradiation time, the  $\cdot\text{OH}$  yields determined from the photoluminescence intensity turn out to be in the order of  $\text{HZOS}_6 < \text{HZOS}_4\text{A}_4 < \text{HZOS}_4 < \text{ZOSA}_4\text{-ET} < \text{HZOS}_4\text{A}_4$ . From Fig. S12b, it can be learned that both the holes in the VB of ZnO and ZnS can react with  $\text{H}_2\text{O}$  and  $\text{OH}^-$  to produce  $\cdot\text{OH}$  because their VB positions (2.89 and 2.56 eV, respectively) are more positive than E ( $\cdot\text{OH}/\text{OH}^-$ ) (+2.38 V vs. NHE) and E( $\cdot\text{OH}/\text{H}_2\text{O}$ ) (+2.27 V vs. NHE).  $\text{HZOS}_6$  was consisted of single ZnS because ZnO core had been completely removed due to the etching.  $\text{HZOS}_6\text{A}_4$  displayed higher  $\cdot\text{OH}$  generated ability than  $\text{HZOS}_6$ , which can be ascribe to the Au NPs deposited on the surface of ZnS.  $\text{HZOS}_4$  generated more  $\cdot\text{OH}$  than  $\text{HZOS}_6\text{A}_4$ , which can be ascribed the formation of traditional II-type heterojunction between ZnS and ZnO, facilitating the separation and migration of electrons and holes [22,23]. Compared with  $\text{HZOS}_4$ , ZOSA<sub>4</sub>-ET exhibited a stronger ability for  $\cdot\text{OH}$  generation, which can also be ascribed to the contributions from Au NPs. It should be noticed that  $\text{HZOS}_4\text{A}_4$  displayed much higher  $\cdot\text{OH}$  generation ability than ZOSA<sub>4</sub>-ET. The difference between  $\text{HZOS}_4\text{A}_4$  and ZOSA<sub>4</sub>-ET can be traced back to the fabrication strategy. During the preparation of  $\text{HZOS}_4\text{A}_4$ , ZnO@ZnS was first etched to produce the hollow channel structure and then deposited with Au NPs. Thus, Au NPs can be deposited from the outer surface, and the  $\text{HAuCl}_4$  solution infiltrating into the hollow channel can be deposited as Au NPs from the inner surface, which forms two interfaces including Au of ZnO-Au-ZnS and ZnS-Au (Fig. 3d-1, d-2). As to ZOSA<sub>4</sub>-ET, ZnO@ZnS was first deposited with Au

NPs and then etched to produce the hollow channel structure. It is very difficult for Au NPs to pass through the thick ZnS layer and deposit at the interface of ZnO and ZnS to form ZnO-Au-ZnS (We failed to find the ZnO-Au-ZnS structure similar to Fig. 3d-1 in the TEM images (Fig. S13) of ZOSA<sub>4</sub>-ET). Therefore, the significantly enhanced  $\cdot\text{OH}$  generation ability of  $\text{HZOS}_4\text{A}_4$  can be ascribed to the Au NPs located at the interface between ZnO and ZnS. It has been widely reported that, when Au NPs are located at the interface between two semiconductors, an indirect Z-scheme transfer mechanism of charge carriers will form among them [29,40,47,49]. The photogenerated electrons in the CB of ZnO are transferred to the VB of ZnS via Au NPs and then quenched with the holes generated by ZnS [25,29,59]. The electrons in the CB of ZnS are quickly captured by Au NPs deposited on the surface of ZnS under the drive force resulted from Schottky barrier, and then reduce  $\text{H}^+$  into  $\text{H}_2$  [42,45,48].

The  $\text{H}_2$  evolution activity over  $\text{HZOS}_4\text{A}_4$  and ZOSA<sub>4</sub>-ET were compared to further investigate the role of the Au NPs between ZnO and ZnS. As shown in Fig. S14b, the  $\text{H}_2$  evolution performance of ZOSA<sub>4</sub>-ET was far lower than that of  $\text{HZOS}_4\text{A}_4$  although  $\text{HZOS}_4\text{A}_4$  and ZOSA<sub>4</sub>-ET shared a similar light absorption property (Fig. S14a), so the enhanced photocatalytic activity of  $\text{HZOS}_4\text{A}_4$  can be ascribed to the Au NPs between ZnO and ZnS, which service as a mediator of transferred electron to accelerate the migration and separation of charge carriers, and thus facilitating the generation of  $\text{H}_2$ . Furthermore, the role of surface Au was further verified by adding 1 wt% Pt as cocatalyst on the  $\text{HZOS}_4\text{A}_4$  sample. As shown Fig. S15, the adding of 1 wt% Pt resulted in a slight decline in the  $\text{H}_2$  generation ability. The decline demonstrates that the Au NPs deposited on the surface of ZnS played the role of cocatalyst, and the addition of 1 wt% Pt caused the over-existence of cocatalysts which shielded some reaction active sites of  $\text{HZOS}_4\text{A}_4$ , resulting in a lower  $\text{H}_2$  evolution rate.

In order to clarify more clearly the roles of the hollow channel structure and the deposited Au NPs, the separation and transfer of charge carriers among these samples with/without hollow channel structure and with/without Au decoration are systematically compared and summarized. As illustrated in Scheme 3a, due to the formation of heterostructure in the ZOS-40, the photogenerated electrons transfer from the VB of ZnS to the VB of ZnO following the traditional II-type mechanism, and then split  $\text{H}_2\text{O}$  into  $\text{H}_2$  at the surface of ZnO. After a part of ZnO core is hollowed out, the transfer mechanism of charge carriers remains unchanged. However, the hollow channel structure

facilitates  $\text{H}_2\text{O}$  to flow in, which helps to quickly consume the photo-generated electrons accumulated on the surface of residual  $\text{ZnO}$  to trigger hydrogen evolution reaction (Scheme 3c). After ZOS-40 is decorated with Au NPs, the transfer mechanism of charge carriers between  $\text{ZnS}$  shell and  $\text{ZnO}$  core still follows the traditional II-type mechanism (Scheme 3b), but the Au NPs deposited on the surface of  $\text{ZnS}$  also promote electron transfer from  $\text{ZnS}$  to Au NPs due to the Schottky junction. As regard to  $\text{HZOS}_4\text{A}_4$  (Scheme 3d), the hollow channel structure and the deposited Au NPs cause synergistic effects on the photocatalytic hydrogen production. Water infiltrating into the hollow channel structure helps to rapidly consume electrons and then produce hydrogen, and the Au NPs located at the interface between  $\text{ZnO}$  and  $\text{ZnS}$  serve as electron shuttles to construct an indirect Z-scheme transfer mechanism, while the Au NPs deposited on the surface of  $\text{ZnS}$  promote electron transfer from  $\text{ZnS}$  to Au NPs because of Schottky junction.

#### 4. Conclusions

In summary, Au NPs decorated flower-like hollow  $\text{ZnO}@\text{ZnS}$  ( $\text{HZOS}$ ) was successfully fabricated for the first time by three sequential procedure, in-situ sulfurization of  $\text{ZnO}$  to form  $\text{ZnO}@\text{ZnS}$ , the etching of  $\text{ZnO}@\text{ZnS}$  to construct hollow channel, the chemical deposition of Au NPs to realize the heterostructure. The size of hollow structure and the loading amount of Au NPs could be precisely controlled by the concentration of KOH and the adding amount of Au precursor. The optimal Au decorated  $\text{HZOS}$  ( $\text{HZOS}_4\text{A}_4$ ) exhibited the highest  $\text{H}_2$  generation rate of 569.81  $\mu\text{mol}/\text{h}$  (10 mg of catalyst was used for photocatalytic reaction), which were one to two orders of magnitude higher than the pure  $\text{ZnO}$ ,  $\text{ZnS}$  or  $\text{ZnO}@\text{ZnS}$  samples. The artful design in hollow channel structure and metal deposition played crucial roles in the facilitation of photocatalytic hydrogen evolution. The hollow channel not only provides sufficient surface active sites but also accelerates the quick migration and separation of both charge carriers and reactant and product molecules. The deposited Au NPs at the interface of  $\text{ZnO}$  and  $\text{ZnS}$  worked as electron shuttles to construct an indirect Z-scheme transfer mechanism, while the Au NPs deposited on the surface of  $\text{ZnS}$  facilitated the directional migration and separation of charge carriers due to Schottky junction. The synergistic effects of hollow channel structure and difunctional Au in the promotion of photocatalytic hydrogen evolution may provide a paradigm in the structure of ingredient design of high efficient heterostructure photocatalyst.

#### Conflict of interest

The authors declare no conflict of interest.

#### Acknowledgments

This work was sponsored by the National Natural Science Fund Committee-Baosteel Group Corporation Steel Joint Research Fund, China (U1460105), the Opening Project of State Key Laboratory of Crystal Materials, Shandong University, China (KF1710), the Opening Project of State Key Laboratory of Physical Chemistry of Solid Surfaces, Xiamen University, China (201715), the State Key Laboratory of Electrical Insulation and Power Equipment, Xi'an Jiaotong University, China (EIP18311). TEM and EDS mapping were carried out at International Center for Dielectric Research (ICDR). SEM and ICP-MS were carried out at Analysis and Test Center of Xi'an Jiaotong University. We thank Chuansheng Ma, Lu Lu, Zijun Ren and Guoqing Zhou for their help in using EDS, TEM, SEM and ICP-MS analyses, respectively.

#### Appendix A. Supplementary data

Supplementary material related to this article can be found, in the online version, at doi:<https://doi.org/10.1016/j.apcatb.2018.12.016>.

#### References

- [1] T. Sun, J. Song, J. Jia, X. Li, X. Sun, Real roles of perylene-tetracarboxylic diimide for enhancing photocatalytic  $\text{H}_2$ -production, *Nano Energy* 26 (2016) 83–89.
- [2] B. Qiu, Q. Zhu, M. Du, L. Fan, M. Xing, J. Zhang, Efficient solar light harvesting  $\text{CdS}/\text{Co}_2\text{S}_8$  hollow cubes for Z-scheme photocatalytic water splitting, *Angew. Chem.* 129 (2017) 2728–2732.
- [3] Z. Chai, T. Zeng, Q. Li, L. Lu, W. Xiao, D. Xu, Efficient visible light-driven splitting of alcohols into hydrogen and corresponding carbonyl compounds over a Ni-modified  $\text{CdS}$  photocatalyst, *Adv. Energy Mater.* 138 (2016) 10128–10131.
- [4] F. Zhang, X. Li, Q. Zhao, Q. Zhang, M. Tadé, S. Liu, Fabrication of  $\alpha\text{-Fe}_2\text{O}_3/\text{In}_2\text{O}_3$  composite hollow microspheres: a novel hybrid photocatalyst for toluene degradation under visible light, *J. Colloid Interface Sci.* 457 (2015) 18–26.
- [5] B. Wu, D. Liu, S. Mubeen, T.T. Chuong, M. Moskovits, G.D. Stucky, Anisotropic growth of  $\text{TiO}_2$  onto gold nanorods for plasmon-enhanced hydrogen production from water reduction, *J. Am. Chem. Soc.* 138 (2016) 1114–1117.
- [6] T. Xiong, W. Cen, Y. Zhang, F. Dong, Bridging the  $\text{g-C}_3\text{N}_4$  interlayers for enhanced photocatalysis, *ACS Catal.* 6 (2015) 2462–2472.
- [7] F. Wang, Y. Sun, Y. He, L. Liu, J. Xu, X. Zhao, G. Yin, L. Zhang, S. Li, Q. Mao, Y. Huang, T. Zhang, B. Liu, Highly efficient and durable  $\text{MoNiNC}$  catalyst for hydrogen evolution reaction, *Nano Energy* 37 (2017) 1–6.
- [8] R. Ye, H. Fang, Y. Zheng, N. Li, Y. Wang, X. Tao, Fabrication of  $\text{CoTiO}_3/\text{g-C}_3\text{N}_4$  hybrid photocatalysts with enhanced  $\text{H}_2$  evolution: Z-scheme photocatalytic mechanism insight, *ACS Appl. Mat. Interfaces* 8 (2016) 13879–13889.
- [9] F.Q. Zhou, J.C. Fan, Q.J. Xu, Y.L. Min,  $\text{BiVO}_4$  nanowires decorated with  $\text{CdS}$  nanoparticles as Z-scheme photocatalyst with enhanced  $\text{H}_2$  generation, *Appl. Catal. B* 201 (2017) 77–83.
- [10] C. Baslak, E. Aslan, I.H. Patir, M. Kus, M. Ersoz, Photocatalytic hydrogen evolution based on mercaptopropionic acid stabilized  $\text{CdS}$  and  $\text{CdTeS}$  quantum dots, *Int. J. Hydrogen Energy* 41 (2016) 20523–20528.
- [11] F. Ma, Y. Wu, Y. Shao, Y. Zhong, J. Lv, X. Hao, 0D/2D nanocomposite visible light photocatalyst for highly stable and efficient hydrogen generation via re-crystallization of  $\text{CdS}$  on  $\text{MoS}_2$  nanosheets, *Nano Energy* 27 (2016) 466–474.
- [12] F. Huang, J. Hou, H. Wang, H. Tang, Z. Liu, L. Zhang, Q. Zhang, S. Peng, J. Liu, G. Cao, Impacts of surface or interface chemistry of  $\text{ZnSe}$  passivation layer on the performance of  $\text{CdS}/\text{CdSe}$  quantum dot sensitized solar cells, *Nano Energy* 32 (2017) 433–440.
- [13] Z. Chai, T. Zeng, Q. Li, L. Lu, W. Xiao, D. Xu, Efficient visible light-driven splitting of alcohols into hydrogen and corresponding carbonyl compounds over a Ni-modified  $\text{CdS}$  photocatalyst, *J. Am. Chem. Soc.* 138 (2016) 10128–10131.
- [14] H. Zhang, G. Liu, L. Shi, J. Ye, Single-atom catalysts: emerging multifunctional materials in heterogeneous catalysis, *Adv. Energy Mater.* 8 (2018) 1701343.
- [15] S. Mukhopadhyay, I. Mondal, U. Pal, P.S. Devi, Fabrication of hierarchical  $\text{ZnO}/\text{CdS}$  heterostructured nanocomposites for enhanced hydrogen evolution from solar water splitting, *Phys. Chem. Chem. Phys.* 17 (2015) 20407–20415.
- [16] Z. Shen, G. Chen, Q. Wang, Y. Yu, C. Zhou, Y. Wang, Sonochemistry synthesis and enhanced photocatalytic  $\text{H}_2$ -production activity of nanocrystals embedded in  $\text{CdS}/\text{ZnS}/\text{In}_2\text{S}_3$  microspheres, *Nanoscale* 4 (2012) 2010–2017.
- [17] H. He, J. Lin, W. Fu, X. Wang, H. Wang, Q. Zeng, Q. Gu, Y. Li, C. Yan, B.K. Tay, C. Xue, X. Hu, S.T. Pantelides, W. Zhou, Z. Liu,  $\text{MoS}_2/\text{TiO}_2$  Edge-on heterostructure for efficient photocatalytic hydrogen evolution, *Adv. Energy Mater.* 6 (2016) 1600464.
- [18] H. Li, Y. Zhou, W. Tu, J. Ye, Z. Zou, State-of-the-art progress in diverse heterostructured photocatalysts toward promoting photocatalytic performance, *Adv. Funct. Mater.* 25 (2015) 998–1013.
- [19] D. Lin, H. Wu, R. Zhang, W. Zhang, W. Pan, Facile synthesis of heterostructured  $\text{ZnO-ZnS}$  nanocables and enhanced photocatalytic activity, *J. Am. Ceram. Soc.* 93 (2010) 3384–3389.
- [20] Z. Wang, S. Cao, S.C.J. Loo, C. Xue, Nanoparticle heterojunctions in  $\text{ZnS-ZnO}$  hybrid nanowires for visible-light-driven photocatalytic hydrogen generation, *CrystEngComm* 15 (2013) 5688–5693.
- [21] D. Bao, P. Gao, X. Zhu, S. Sun, Y. Wang, X. Li, Y. Chen, H. Zhou, Y. Wang, P. Yang,  $\text{ZnO}/\text{ZnS}$  heterostructured nanorod arrays and their efficient photocatalytic hydrogen evolution, *Chem-Eur. J.* 21 (2015) 12728–12734.
- [22] D. Wu, Y. Jiang, Y. Yuan, J. Wu, K. Jiang,  $\text{ZnO-ZnS}$  heterostructures with enhanced optical and photocatalytic properties, *J. Nanopart. Res.* 12 (2011) 2875–2886.
- [23] W. Chen, H. Ruan, Y. Hu, D. Li, Z. Chen, J. Xian, J. Chen, X. Fu, Y. Shao, Y. Zheng, One-step preparation of hollow  $\text{ZnO}$  core/ $\text{ZnS}$  shell structures with enhanced photocatalytic properties, *CrystEngComm* 14 (2012) 6295–6305.
- [24] S.Y. Cheon, J. Yoon, K.H. Oh, K.Y. Jang, J.H. Seo, J.Y. Park, S. Choi, W.S. Seo, G. Lee, K.M. Nam, Sonochemical synthesis of  $\text{ZnO-ZnS}$  core-shell nanorods for enhanced photoelectrochemical water oxidation, *J. Am. Chem. Soc.* 100 (2017) 3825–3834.
- [25] J. Han, Z. Liu, K. Guo, B. Wang, X. Zhang, T. Hong, High-efficiency photoelectrochemical electrodes based on  $\text{ZnIn}_2\text{S}_4$  sensitized  $\text{ZnO}$  nanotube arrays, *Appl. Catal. B* 163 (2015) 179–188.
- [26] D. Chen, Z. Liu, M. Zhou, P. Wu, J. Wei, Enhanced photoelectrochemical water splitting performance of  $\alpha\text{-Fe}_2\text{O}_3$  nanostructures modified with  $\text{Sb}_2\text{S}_3$  and cobalt phosphate, *J. Alloy. Compounds* 742 (2018) 918–927.
- [27] Y. Zou, J. Shi, D. Ma, Z. Fan, C. Niu, L. Wang, Fabrication of  $\text{g-C}_3\text{N}_4/\text{Au-C-TiO}_2$  hollow structures as visible-light-driven Z-scheme photocatalysts with enhanced photocatalytic  $\text{H}_2$  evolution, *ChemCatChem* 9 (2017) 3752–3761.
- [28] C. Marchal, T. Cottineau, M.G. Méndez-Medrano, C. Colbeau-Justin, V. Caps, V. Keller,  $\text{Au/TiO}_2\text{-g-C}_3\text{N}_4$  nanocomposites for enhanced photocatalytic  $\text{H}_2$  production from water under visible light irradiation with very low quantities of

sacrificial agents, *Adv. Energy Mater.* (2018) 1702142.

[29] J. Zhang, Z. Liu, Z. Liu, Novel  $\text{WO}_3/\text{Sb}_2\text{S}_3$  heterojunction photocatalyst based on  $\text{WO}_3$  of different morphologies for enhanced efficiency in photoelectrochemical water splitting, *ACS Appl. Mater. Interfaces* 8 (2016) 9684–9691.

[30] P. Li, Z. Wei, T. Wu, Q. Peng, Y. Li, Influence of gold core concentration on visible photocatalytic activity of golde zinc sulfide core-shell nanoparticle, *J. Power Sources* 294 (2015) 580–587.

[31] J. Zhang, Y. Wang, J. Zhang, Z. Lin, F. Huang, J. Yu, Enhanced photocatalytic hydrogen production activities of Au loaded  $\text{ZnS}$  flowers, *ACS Appl. Mater. Interfaces* 5 (2013) 1031–1037.

[32] Y. Liu, Y. Gu, X. Yan, Z. Kang, S. Lu, Y. Sun, Y. Zhang, Design of sandwich-structured  $\text{ZnO}/\text{ZnS}/\text{Au}$  photoanode for enhanced efficiency of photoelectrochemical water splitting, *Nano Res.* 8 (2015) 2891–2900.

[33] Y. Zou, J. Shi, D. Ma, Z. Fan, L. Lu, C. Niu, In situ synthesis of C-doped  $\text{TiO}_2@g-\text{C}_3\text{N}_4$  core-shell hollow nanospheres with enhanced visible-light photocatalytic activity for  $\text{H}_2$  evolution, *Chem. Eng. J.* 322 (2017) 435–444.

[34] D. Ma, J. Shi, Y. Zou, Z. Fan, X. Ji, C. Niu, Highly efficient photocatalyst based on a CdS quantum Dots/ZnO nanosheets 0D/2D heterojunction for hydrogen evolution from water splitting, *ACS Appl. Mater. Interfaces* 9 (2017) 25377–25386.

[35] J. Shi, D. Ma, Y. Zou, Z. Fan, J. Shi, L. Cheng, X. Ji, C. Niu, Rational construction of multiple interfaces in ternary heterostructure for efficient spatial separation and transfer of photogenerated carriers in the application of photocatalytic hydrogen evolution, *J. Power Sources* 379 (2018) 249–260.

[36] C. Miao, G. Y. A. B. A., X. Lu, L. Zhao, W. Guo, Q. Xue, Preparation of large diameter and low density  $\text{ZnS}$  microtube arrays via a sacrificial template method, *Mater. Lett.* 115 (2014) 140–143.

[37] H. Zhao, Y. Dong, P. Jiang, X. Wu, R. Wu, Y. Chen, Facile preparation of a  $\text{ZnS}/\text{ZnO}$  nanocomposite for robust sunlight photocatalytic  $\text{H}_2$  evolution from water, *RSC Adv.* 5 (2015) 6494–6500.

[38] Z.B. Yu, Y.P. Xie, G. Liu, G.Q.M. Lu, X.L. Ma, A.H. Cheng, Self-assembled CdS/Au/ZnO heterostructure induced by surface polar charges for efficient photocatalytic hydrogen evolution, *J. Mater. Chem. A Mater. Energy Sustain.* 1 (2013) 2773–2776.

[39] W. He, H. Kim, W.G. Wamer, D. Melka, J.H. Callahan, J. Yin, Photogenerated charge carriers and reactive oxygen species in  $\text{ZnO}/\text{Au}$  hybrid nanostructures with enhanced photocatalytic and antibacterial activity, *J. Am. Chem. Soc.* 136 (2014) 750–757.

[40] M. Cao, P. Wang, Y. Ao, V. Wang, J. Hou, J. Qian, Investigation on graphene and Pt Co-modified CdS nanowires with enhanced photocatalytic hydrogen evolution activity under visible light irradiation, *Dalton Trans.* 44 (2015) 16372–16382.

[41] F. Wang, Z. Jin, Y. Jiang, E.H.G. Backus, M. Bonn, S.N. Lou, D. Turchinovich, R. Amal, Probing the charge separation process on  $\text{In}_2\text{S}_3/\text{Pt}-\text{TiO}_2$  nanocomposites for boosted visible-light photocatalytic hydrogen production, *Appl. Catal. B* 198 (2016) 25–31.

[42] D. Ma, J. Shi, Y. Zou, Z. Fan, X. Ji, C. Niu, L. Wang, Rational design of CdS@ZnO core-shell structure via atomic layer deposition for drastically enhanced photocatalytic  $\text{H}_2$  evolution with excellent photostability, *Nano Energy* 39 (2017) 183–191.

[43] S.Y. Cheon, J. Yoon, K.H. Oh, K.Y. Jang, J.H. Seo, J.Y. Park, S. Choi, W.S. Seo, G. Lee, K.M. Nam, Sonochemical synthesis of  $\text{ZnO}-\text{ZnS}$  core-shell nanorods for enhanced photoelectrochemical water oxidation, *J. Am. Chem. Soc.* 100 (2017) 3825–3834.

[44] Q. Chen, S. Wu, Y. Xin, Synthesis of  $\text{Au}-\text{CuS}-\text{TiO}_2$  nanobelts photocatalyst for efficient photocatalytic degradation of antibiotic oxytetracycline, *Chem. Eng. J.* 302 (2016) 377–387.

[45] W. Li, C. Feng, S. Dai, J. Yue, F. Hua, H. Hou, Fabrication of sulfur-doped  $g-\text{C}_3\text{N}_4/\text{Au}/\text{CdS}$  Z-scheme photocatalyst to improve the photocatalytic performance under visible light, *Appl. Catal. B* 168–169 (2015) 465–471.

[46] N.A.H. Kareem, N.M. Jassim, Second- Harmonic Generation Improved of  $\text{ZnS}/\text{Au}$  Core/Shell Nanomaterials, *Natural Sci. Res.* 8 (2018) 38–42.

[47] X. Ding, Y.J. Li, Y. Zhao, Y. Zhu, W. Li, C. Deng, Wang, Enhanced photocatalytic  $\text{H}_2$  evolution over  $\text{CdS}/\text{Au}/g-\text{C}_3\text{N}_4$  composite photocatalyst under visible-light irradiation, *Appl. Materials* 3 (2015) 104410.

[48] W. Jo, T. Sivakumar Natarajan, Facile synthesis of novel redox-mediator-free direct Z-scheme  $\text{CaIn}_2\text{S}_4$  marigold-flower-like/ $\text{TiO}_2$  photocatalysts with superior photocatalytic efficiency, *ACS Appl. Mater. Interfaces* 7 (2015) 17138–17154.

[49] X. Yue, S. Yi, R. Wang, Z. Zhang, S. Qiu, Synergistic effect based  $\text{Ni}_x\text{Co}_{1-x}$  architected  $\text{Zn}_{0.75}\text{Cd}_{0.25}\text{S}$  nanocrystals: an ultrahigh and stable photocatalysts for hydrogen evolution from water splitting, *Appl. Catal. B* 224 (2018) 17–26.

[50] S. Liu, C. Li, J. Yu, Q. Xiang, Improved visible-light photocatalytic activity of porous carbon self-doped  $\text{ZnO}$  nanosheet-assembled flowers, *CrystEngComm* 13 (2011) 2533–2541.

[51] J. Xu, Z. Chen, J.A. Zapien, C. Lee, W. Zhang, Surface engineering of  $\text{ZnO}$  nanostructures for semiconductor-sensitized solar cells, *Adv. Mater.* 26 (2014) 5337–5367.

[52] J. Xu, H. Sang, X. Wang, K. Wang, Facile synthesis and photocatalytic properties of  $\text{ZnO}$  core/ $\text{ZnS}-\text{CdS}$  solid solution shell nanorods grown vertically on reductive graphene oxide, *Dalton Trans.* 44 (2015) 9528–9537.

[53] Z. Wang, W. Wu, Q. Xu, G. Li, S. Liu, X. Jia, Y. Qin, Z.L. Wang, Type-II heterojunction dual shell hollow spheres loaded with spatially separated cocatalyst for enhancing visible light hydrogen evolution, *Nano Energy* 38 (2017) 518–525.

[54] L. Chen, W. Zhang, C. Feng, Z. Yang, Y. Yang, Replacement/etching route to  $\text{ZnSe}$  nanotube arrays and their enhanced photocatalytic activities, *Ind. Eng. Chem. Res.* 51 (2012) 4208–4214.

[55] F. Ning, M. Shao, S. Xu, Y. Fu, R. Zhang, M. Wei, D.G. Evans, X. Duan,  $\text{TiO}_2$ /graphene/NiFe-layered double hydroxide nanorods array photoanodes for efficient photoelectrochemical water splitting, *Energy Environ. Sci.* 9 (2016) 2633–2643.

[56] Z. Liu, J. Zhang, W. Yan, Enhanced photoelectrochemical water splitting of photoelectrode simultaneous decorated with cocatalysts based on spatial charge separation and transfer, *ACS Sustain. Chem. Eng.* 6 (2018) 3565–3574.

[57] S. Bai, J. Jiang, Q. Zhang, Y. Xiong, Steering charge kinetics in photocatalysis: intersection of materials syntheses, characterization techniques and theoretical simulations, *Chem. Soc. Rev.* 44 (2015) 2893–2939.

[58] D. Ding, K. Liu, S. He, C. Gao, Y. Yin, Ligand-exchange assisted formation of  $\text{Au}/\text{TiO}_2$  schottky contact for visible-light photocatalysis, *Nano Lett.* 14 (2014) 6731–6736.

[59] F. Ye, H. Li, H. Yu, S. Chen, X. Quan, Constructing  $\text{BiVO}_4-\text{Au}@\text{CdS}$  photocatalyst with energetic charge-carrier separation capacity derived from facet induction and Z-scheme bridge for degradation of organic pollutants, *Appl. Catal. B* 227 (2018) 258–265.